[Supporting Information]

Heterogeneity in Dynamic Metamolecules

Sunghee Lee,[†,‖] *Omar Ibrahim,*[‡,‖] *Zahra Fakhraai,*[*,‡] *and So-Jung Park*[*,†]

† Department of Chemistry and Nanoscience, Ewha Womans University, 52 Ewhayeodae-gil, Seodaemun-gu, Seoul 03760, Korea

‡ Department of Chemistry, University of Pennsylvania, 231 South 34th Street, Philadelphia, Pennsylvania 19104, United States

*Corresponding Authors: sojungpark@ewha.ac.kr (So-Jung Park), fakhraai@sas.upenn.edu (Zahra Fakhraai)

‖ These authors contributed equally.

KEYWORDS

Plasmonic, Metal nanoparticles, Heterogeneity, Magnetic resonance, Metamaterial, Dynamic nanostructure, PNIPAM

I. Detailed Experimental Procedures

Materials. Gold(III) chloride trihydrate ($HAuCl_4 \cdot 3H_2O$, ≥99.9%), silver nitrate ($AgNO_3$, 99.9999%), trisodium citrate dehydrate (≥99%), tannic acid (≥99.5%), *N,N'*-methylene bis-(acrylamide) (99%), allylamine (98%), and potassium persulfate (99%) were purchased from Sigma-Aldrich. *N*-Isopropylacrylamide (98%) was purchased from Wako Chemical Ltd. (Japan). All chemicals were used without purification.

Synthesis of plasmonic metal nanobeads. Au nanobeads were synthesized by a modified citrate reduction method.[1-2] First, 60 mg of $HAuCl_4 \cdot 3H_2O$ was dissolved in 196 mL ultra-pure water (18.2 MΩ), and the solution was heated with an oil bath in a 500 mL one-neck round-bottom flask under vigorous stirring. After boiling, 4 mL of 0.18 M sodium citrate solution was quickly injected. The color of the solution changed from pale yellow to purple and then red within 5 min. After 15 min, the nanobead solution was cooled to room temperature and kept in a refrigerator. This procedure generates Au nanobeads with a diameter of 12.7 ± 0.9 nm. Larger Au nanobeads were synthesized by the serial growth method. The 12.7 nm Au nanobead solution was heated to 90 °C and equilibrated at that temperature for 10 min. Then, 0.5 mL of 60 mM sodium citrate solution and 0.5 mL of a 25 mM $HAuCl_4 \cdot 3H_2O$ solution were sequentially injected into a nanoparticle solution with less than a 2 min interval. Au nanobeads with various diameters were synthesized by repeating the process. Silver nanobeads were prepared by following a previously reported method.[3] Synthesized nanoparticles were washed by centrifugation and redispersed in a 1 mM sodium citrate solution.

Synthesis of Poly(*N*-isopropylacrylamide-*co*-allylamine) PNIPAM hydrogels. PNIPAM hydrogels were synthesized by the precipitation polymerization method, following a literature procedure.[4]

Fabrication of dynamic metamolecules (MMs). Dynamic MMs were prepared by following our previously reported procedure.[5] Freshly prepared Au or Ag nanobeads dispersed in 1 mM sodium citrate solution (4 mL) and 10 μL of 1 wt% PNIPAM hydrogel solution were mixed in a 10 mL glass vial. This solution was kept at room temperature for about 24 h for small nanobeads and for 12 h for large nanobeads (> 40 nm). Afterwards, this solution was purified from unattached nanobeads for further use. The number of nanobeads on a PNIPAM hydrogel was controlled by varying the concentration of the nanobead solution as indicated in Table S2.

Fabrication of dynamic binary metamolecules (BMMs) with two different diameters of Ag nanobeads. The preparation of BMMs with two different diameters of Ag nanobeads is similar to that of Au BMMs. Freshly prepared 45 nm Ag beads dispersed in a 1 mM sodium citrate solution (2 mL) and 10 μL of a 1 wt% PNIPAM hydrogel solution were mixed in a 10 mL glass vial. This solution was stirred for 3 h under vigorously mixing. Afterwards, 0.80 nM of 16 nm Ag beads dispersed in 1 mM sodium citrate solution (2 mL) was added to each Ag45 MM solution. The mixed solution was stirred at 450 rpm for 30 min and kept undisturbed at room temperature for 12 h. Unattached nanobeads were removed, and the precipitates of BMMs were dispersed in a sodium citrate solution (4 mL, 1 mM). The number of nanobeads on a PNIPAM hydrogel was controlled by varying the concentration of nanobead solutions as indicated in Table S1(4-6).

Characterization. Extinction spectra were measured with an Agilent 8453 UV-Vis spectrometer. Scanning electron microscope (SEM) images were obtained using a JEOL JSM-7610F at an accelerating voltage of 15 kV. Transmission electron microscope (TEM) images were taken with a JEOL JEM-2100F at an accelerating voltage of 200 kV. Dynamic light scattering (DLS) measurements were conducted using a Malvern Zetasizer Nano ZS with a He-Ne laser (633 nm).

TEM and SEM sampling of MMs and BMMs. For l-MMs and l-BMMs, 5 μL of a solution was placed on a TEM grid and silicon wafer at room temperature for TEM and SEM imaging, respectively, which was then dried at room temperature. For h-MMs and h-BMMs, a solution was preheated to 50 °C for 30 min. A silicon wafer was also preheated at 50 °C for several hours in the oven. Then, 5 μL of the preheated solution was placed on the preheated silicon wafer, which was dried in an oven at 50 °C.

II. FDTD Simulation Details

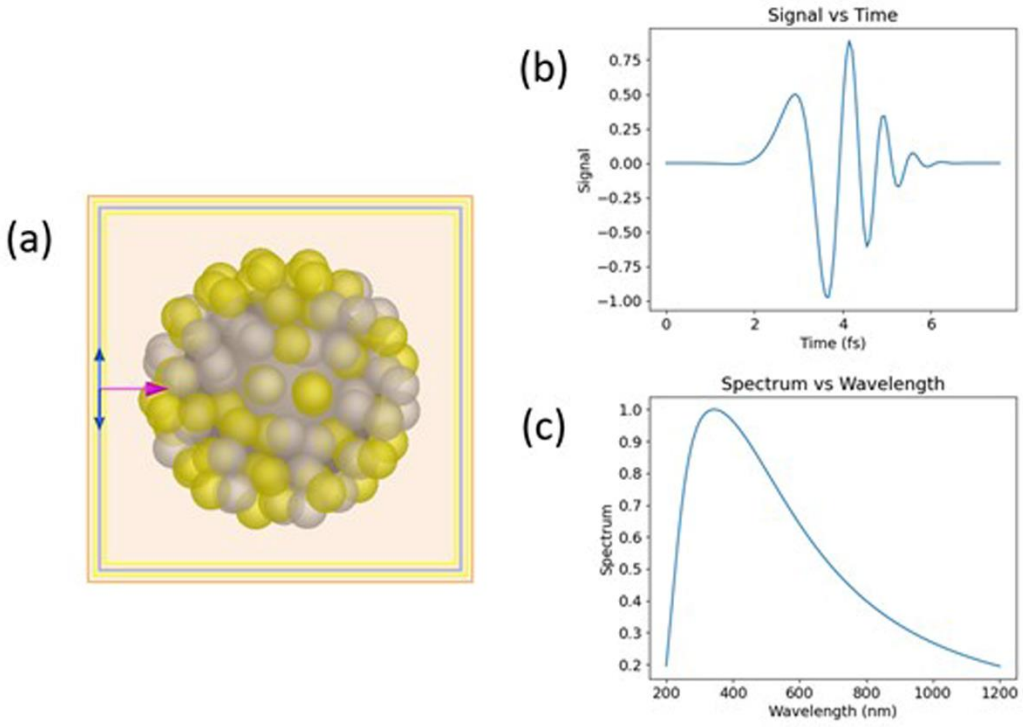

Figure S1. (a) Simulation region for the FDTD region. The TFSF source is in grey, with the pink arrow representing the direction of propagation, while the blue arrows represent the polarization direction. The outer orange box represents the mesh refinement region (which uses a mesh size of 2 nm). The inner yellow box inside the TFSF source represents the absorption monitor, while the outer yellow box between the TFSF source and mesh boundary represents the scattering monitor. (b-c) Information about the pulse used to excite the structure.

FDTD Modal Basis Decomposition. To obtain the strength of each mode in the total scattering cross-section in the FDTD simulation data, we performed a basis decomposition of the scattered electric and magnetic fields obtained from the simulation. We obtained the scattered electric field and magnetic field at all mesh points in a thin shell outside of the TFSF source. It is important that no part of this shell intersects with the source to ensure that the fields at the shell contain only the scattered field, which requires that the distance to the inner edge of the shell be at least a factor of $\sqrt{3}$ from the edges of the source. The shell was centered at a distance R from the center of the structure and was thick enough so that grid interpolation could be used to interpolate the field at any angle (θ, ϕ) at this distance. A sample setup for this simulation is shown in Figure S2. The scattered electric field can then be written:

$$\vec{E}_s(\vec{r}) = \sum_{n=1}^{\infty} \sum_{m=-n}^{n} \left[a_{mn}^{M} \vec{M}(kr, \theta, \phi) + a_{mn}^{N} \vec{N}(kr, \theta, \phi) \right]$$

where $\vec{M}$ and $\vec{N}$ constitute a complete basis and $\vec{M}$ represents the scattered electric field due to magnetic scattering and $\vec{N}$ represents the scattered electric field due to electric scattering.[6] a_{mn}^{M} and a_{mn}^{N} are the associated basis expansion coefficients, respectively. Note that n corresponds to the mode order ($n = 1$: dipole, $n = 2$: quadrupole, etc.), while m corresponds to the given sub mode ($-n \leq m \leq n$). In this work, we only calculate modes up to $n = 3$, which corresponds to octupole modes. Next, a_{mn}^{M} and a_{mn}^{N} were calculated through numerical integration of FDTD data via the following formula:[7-8]

$$a_{mn}^{M} = \frac{i}{c\epsilon_0 N} \frac{\left[\oint \left(\hat{r} \cdot \overrightarrow{H_s}\right) Y_n^{-m}(\theta, \phi) dA\right] k(2n+1)}{4\pi R^2 \gamma_{mn}(-1)^m n(n+1) h_n(kR)}$$

$$a_{mn}^{N} = \frac{\left[\oint \left(\hat{r} \cdot \overrightarrow{E_s}\right) Y_n^{-m}(\theta, \phi) dA\right] k(2n+1)}{4\pi R^2 \gamma_{mn}(-1)^m n(n+1) h_n(kR)}$$

The integration is performed in our sphere of interpolation, and N represents the refractive index of the medium, Y_n^m represents the spherical harmonic of order (n, m), h_n represents the spherical Hankel function, and $\gamma_{mn} \equiv \sqrt{\frac{(2n+1)(n-m)!}{4\pi n(n+1)(n+m)!}}$.[6] After obtaining the basis coefficients, we can then calculate the scattered electric and magnetic field contributions of each electric and magnetic multipole mode at any point in the far field. From here we can use the TFSF intensity I provided by Lumerical and numerically integrate the Poynting vector calculated from the scattered fields to obtain the scattering cross-section of a given mode n:

$$C_{scat} = \frac{1}{2I} \int_{\Omega} Re\left(\vec{E}_{\mathrm{n}} \times \overrightarrow{\mathrm{H}_{\mathrm{n}}^{*}}\right) \cdot d\vec{A}$$

The accuracy of this method was confirmed by verifying that the scattering cross-section of each mode up to and including $n = 3$ sums up to the FDTD total scattering cross-section result.

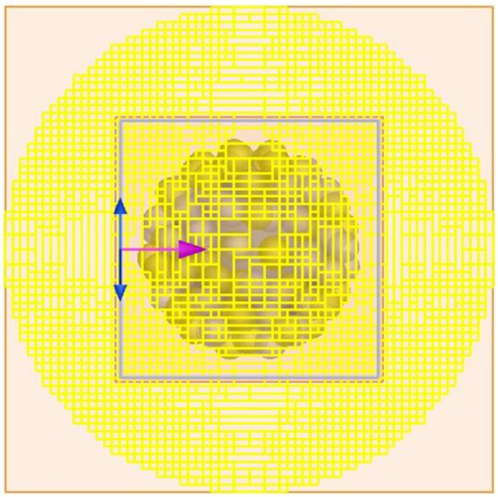

Figure S2. Simulation region for the modal decomposition simulation. A shell monitor was constructed out of smaller rectangular monitors (shown in yellow) that are contained within the outer mesh region (orange) and outside of the TFSF source (grey). An inner, finer mesh region with a mesh size of 2 nm contained the structure (orange box just slightly larger than the TFSF source) while an outer, coarser mesh region with a mesh size of 4 nm was used where the scattered field was collected (outer orange box).

III. Supplementary Data

Table S1. Experimental conditions and structural parameters for dynamic BMMs with two different diameters of nanobeads.

	Material	Small bead diameter (nm)	Large bead diameter (nm)	Concentration of large bead solution[a] (nM)	Number of small beads	Number of large beads	Spectral data
1	Au	15 ± 1	45 ± 2	0.10	163 ± 19	25 ± 5	Figure 1(b magenta, blue), Figure 2(b blue), Figure 3(a blue) Figure S7(a), Figure S9(a blue)
2	Au	15 ± 1	45 ± 2	0.010	163 ± 19	2 ± 2	Figure 2(b red), Figure S9(a red), Figure S11(b)
3	Au	15 ± 1	45 ± 2	0.050	163 ± 19	9 ± 4	Figure 2(b magenta), Figure S9(a magenta), Figure S11(c)
4	Ag	16 ± 2	45 ± 3	0.010	162 ± 23	2 ± 1	Figure S16(a-b red), Figure S19(b)
5	Ag	16 ± 2	45 ± 3	0.050	166 ± 17	10 ± 2	Figure S16(a-b magenta), Figure S19(c)
6	Ag	16 ± 2	45 ± 3	0.13	154 ± 8	28 ± 3	Figure S16(a-b blue), Figure S20(a), Figure S22(b blue)

[a] The concentration of the small bead solution was fixed, and the concentration of the large bead solution was adjusted to control the number of large beads attached to a PNIPAM hydrogel.

Table S2. Experimental conditions and structural parameters for MMs.

	Material	Concentration of bead solution (nM)	Bead diameter (nm)	Number of beads	Spectral data
1	Au	0.40	15 ± 1	163 ± 19	Figure 1(b black), Figure 2(b black), Figure 3(a black) Figure S9(a black), Figure S11(a)
2	Au	0.050	45 ± 2	26 ± 4	Figure 3(a blue dotted)
3	Au	0.10	45 ± 2	61 ± 4	Figure S8(c)
4	Au	0.60	15 ± 1	268 ± 16	Figure S13(c)
5	Ag	0.40	16 ± 2	156 ± 9	Figure S16(a-b black), Figure S19(a), Figure S22(b black)
6	Ag	0.050	45 ± 3	30 ± 2	Figure S22(b blue dotted)
7	Ag	0.075	35 ± 2	45 ± 3	Figure 4(d-e orange), Figure S25(b red)
8	Au	0.075	35 ± 2	44 ± 4	Figure 4(d-e red), Figure S25(c red)
9	Ag	0.18	25 ± 2	76 ± 4	Figure S27(d red), Figure S31(a-b orange)
10	Ag	0.030	45 ± 3	23 ± 4	Figure S28(d red), Figure S31(c-d orange)
11	Au	0.20	25 ± 1	68 ± 6	Figure S31(a-b red)
12	Au	0.030	45 ± 2	20 ± 3	Figure S31(c-d red)
13	Ag	0.30	35 ± 2	86 ± 6	Figure 6(c orange), Figure S33 (a orange), Figure S34(a red)
14	Au	0.30	35 ± 2	85 ± 7	Figure 6(c red), Figure S33 (a red), Figure S34(b red)

Table S3. Simulated structural parameters for Au15 MMs, Au45 MMs, and Au15/Au45 BMMs[a].

	Number of 45 nm beads	Number of 15 nm beads	45 nm-45 nm NN[b] gap distances (nm)	45 nm-15 nm NN gap distances (nm)	15 nm-15 nm NN gap distances (nm)	Spectral data
1	25	163	23.52 ± 1.69	3.89 ± 0.43	3.28 ± 0.64	Figure 1(e-f), Figure 2(c-d blue), Figure 3(d-e blue), Figure S12(a-b blue)
2	0	163	N/A	N/A	8.77 ± 0.50	Figure 2(c-d black), Figure 3(d-e black)
3	2	163	136.53 ± 0	15.81 ± 0.17	8.03 ± 0.55	Figure 2(c-d red)
4	9	163	61.14 ± 3.64	10.89 ± 0.31	5.88 ± 0.58	Figure 2(c-d magenta)
5	25	0	24.82 ± 1.48	N/A	N/A	Figure 3(d-e blue dotted)
6	0	163	N/A	N/A	3.28 ± 0.64	Figure S12(a-b black)
7	25	0	23.52 ± 1.69	N/A	N/A	Figure S12(a-b blue dotted)

[a] The core size of all samples is 155 nm. [b] NN indicates the nearest neighbors.

Table S4. Experimental condition and structural parameters for Au/Ag BMMs.

	Au bead diameter (nm)	Ag bead diameter (nm)	Concentration of bead solution (nM)	Number of Au beads	Number of Ag beads	Sum of beads	Spectral data
1	35 ± 2	35 ± 2	0.15	46 ± 4	37 ± 3	83 ± 5	Figure 4c, Figure 4(d black dashed), Figure 4(e black), Figure 6(c black), Figure S24(a), Figure S25(a red)
2	25 ± 1	25 ± 2	0.20	70 ± 6	68 ± 5	139 ± 9	Figure S27(d magenta, blue), Figure S29(a), Figure S31(a black dashed), Figure S31(b black)
3	45 ± 2	45 ± 3	0.030	20 ± 3	20 ± 2	40 ± 4	Figure S28(d magenta, blue), Figure S29(b), Figure S31(c black dashed), Figure S31(d black)

Table S5. Simulated structural parameters for Au/Ag BMMs.

	Number of Au beads	Number of Ag beads	Core size (nm)	Bead diameter (nm)	NN gap distances (nm)	Au-Au NN gap distances (nm)	Ag-Ag NN gap distances (nm)	Spectral data
1	46	37	175	35	5.97 ± 0.78	7.22 ± 1.83	8.80 ± 6.67	Figure 5(b-d black), Figure 6(d-f black), Figure S25(a black), Figure S25(d,g), Figure S26(a-d black)
2	70	69	175	25	5.22 ± 0.68	6.23 ± 3.42	6.37 ± 3.57	Figure S32(a-c black)
3	20	20	150	45	9.25 ± 0.55	11.46 ± 3.13	10.25 ± 1.81	Figure S32(d-f black)
4	62	21	175	35	5.97 ± 0.78	6.34 ± 1.43	14.80 ± 14.89	Figure S35(a-c navy dashed)
5	21	62	175	35	5.97 ± 0.78	10.36 ± 10.60	6.40 ± 1.57	Figure S35(a-c magenta dashed)

Table S6. Simulated structural parameters for Au MMs and Ag MMs.

	Material	Number of beads	Core size (nm)	Bead size (nm)	NN gap distances (nm)	Spectral data
1	Ag	37	175	35	8.80 ± 6.67	Figure 5(b-d orange), Figure S25(b black), Figure S25(e,h), Figure S26(a-d orange)
2	Au	46	175	35	7.22 ± 1.83	Figure 5(b-d red), Figure S25(c black), Figure S25(f,i), Figure S26(a-d red)
3	Ag	69	175	25	6.37 ± 3.57	Figure S32(a-c orange)
4	Au	70	175	25	6.23 ± 3.42	Figure S32(a-c red)
5	Ag	20	150	45	10.25 ± 1.81	Figure S32(d-f orange)
6	Au	20	150	45	11.46 ± 3.13	Figure S32(d-f red)
7	Ag	83	175	35	5.97 ± 0.78	Figure 6(d-f orange), Figure S34(a black), Figure S34(c,e), Figure S35(a-f orange)
8	Au	83	175	35	5.97 ± 0.78	Figure 6(d-f red), Figure S34(b black), Figure S34(d,f), Figure S35(a-f red)

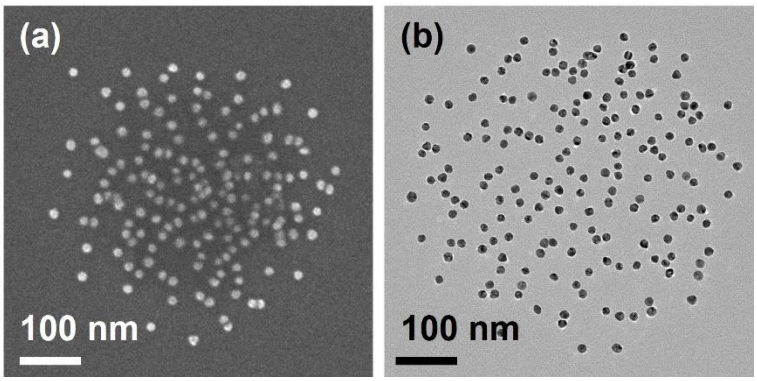

Figure S3. (a-b) SEM (a) and TEM (b) images of Au15 l-MM with a total of 163 ± 19 15 nm Au beads.

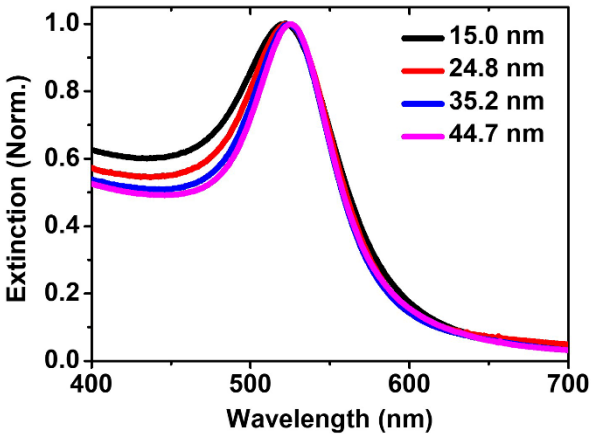

Figure S4. Extinction spectra of Au nanobeads with various diameters.

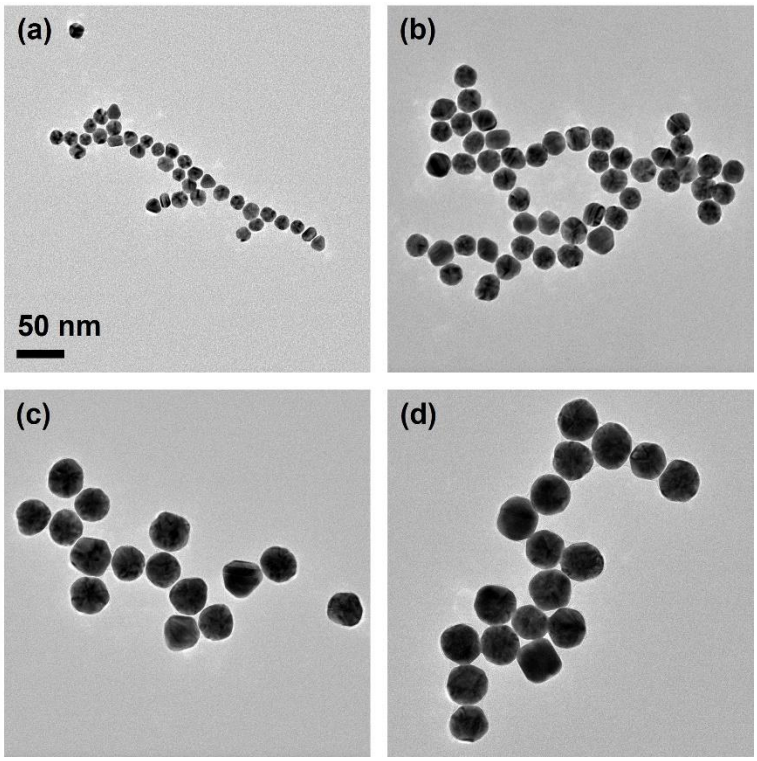

Figure S5. (a-d) TEM images of Au nanobeads with various diameters. The average diameters of nanobeads were measured to be (a) 15 ± 1, (b) 25 ± 1, (c) 35 ± 2, and (d) 45 ± 2 nm.

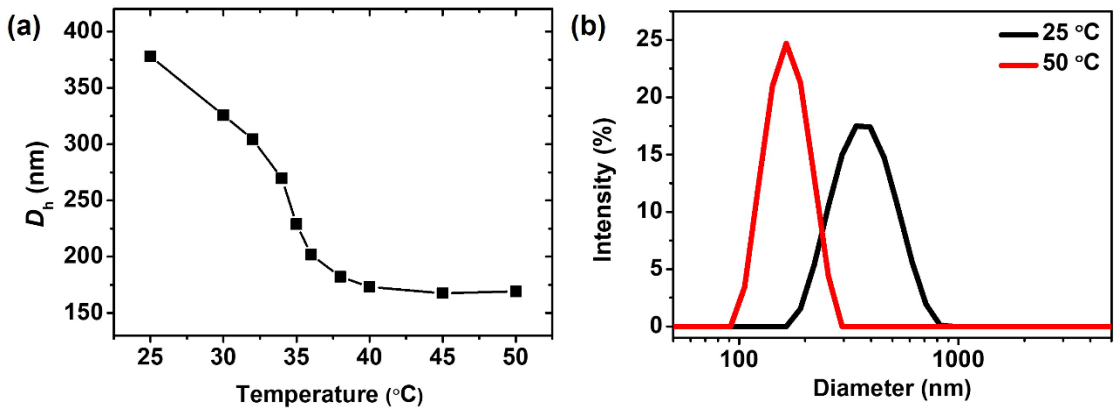

Figure S6. (a) Temperature-dependent hydrodynamic diameter (D_h) of PNIPAM hydrogels. The transition temperature was measured to be 34 °C. (b) DLS data of PNIPAM hydrogels was obtained at 25 and 50 °C. The D_h of PNIPAM hydrogels was measured to be 379 ± 84 nm (polydispersity index (PDI): 0.08) at 25 °C and 169 ± 37 nm (PDI: 0.01) at 50 °C by DLS measurement.

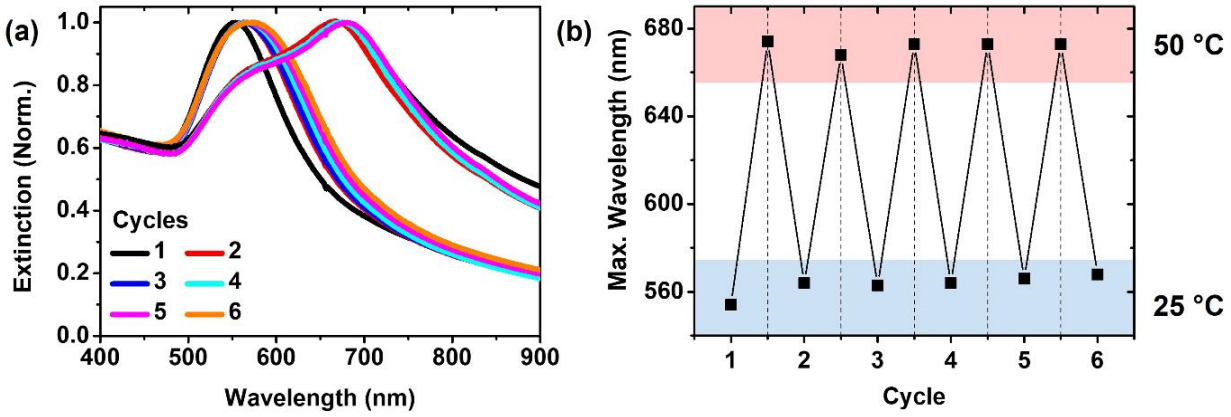

Figure S7. (a) Extinction spectra of Au15/Au45 BMMs with two different diameters of nanobeads measured with temperature cycling between 25 °C and 50 °C. (b) Extinction peak positions corresponding to temperature cycling as shown in a. The slight peak broadening after the heating cooling cycle shown in a can be attributed to the slight reorganization of large nanobeads during the heating process.

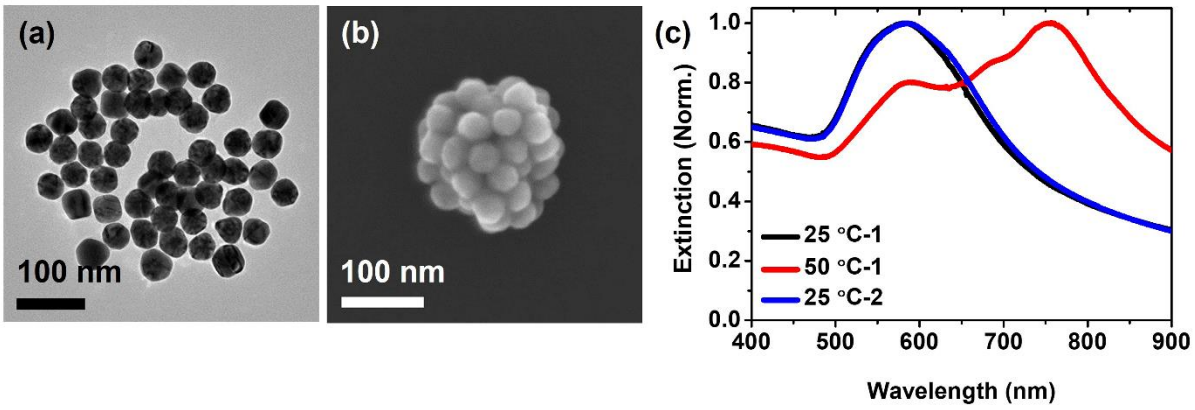

Figure S8. Au45 MMs constructed with 61 ± 4 of 45 nm beads, showing that a large number of 45 nm beads is required to manifest strong magnetic resonances. (a) TEM images of Au45 l-MMs. (b) SEM images of Au45 h-MMs. (c) Extinction spectra measured while varying the temperature from 25 °C (black) to 50 °C (red) and back to 25 °C (blue) for Au45 MMs.

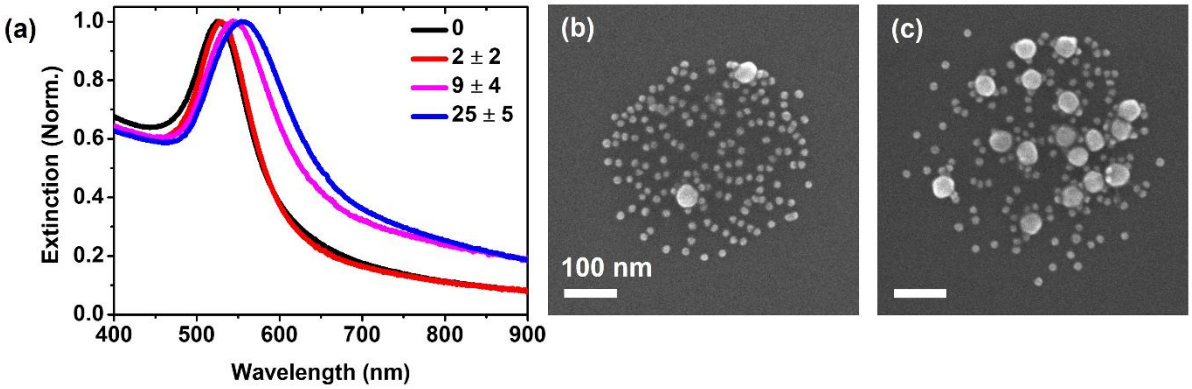

Figure S9. (a) Normalized extinction spectra of Au15/Au45 l-BMMs with two different diameters of Au nanobeads. The legend indicates the number of 45 nm Au beads. (b-c) SEM images of Au15/Au45 l-BMMs constructed with two different diameters of nanobeads. Other structural parameters are summarized in Table S1(2-3).

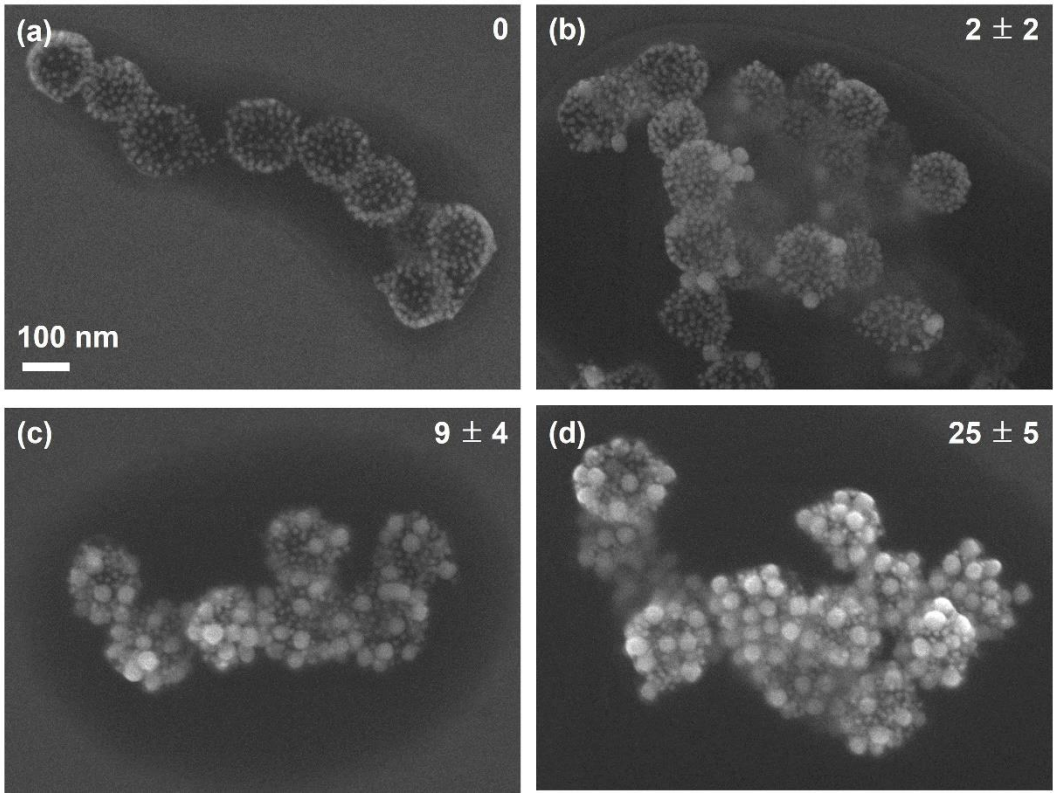

Figure S10. (a-d) SEM images of Au15/Au45 h-BMMs with two different diameters of nanobeads. The numbers in the SEM images indicate the average number of 45 nm beads on a PNIPAM hydrogel.

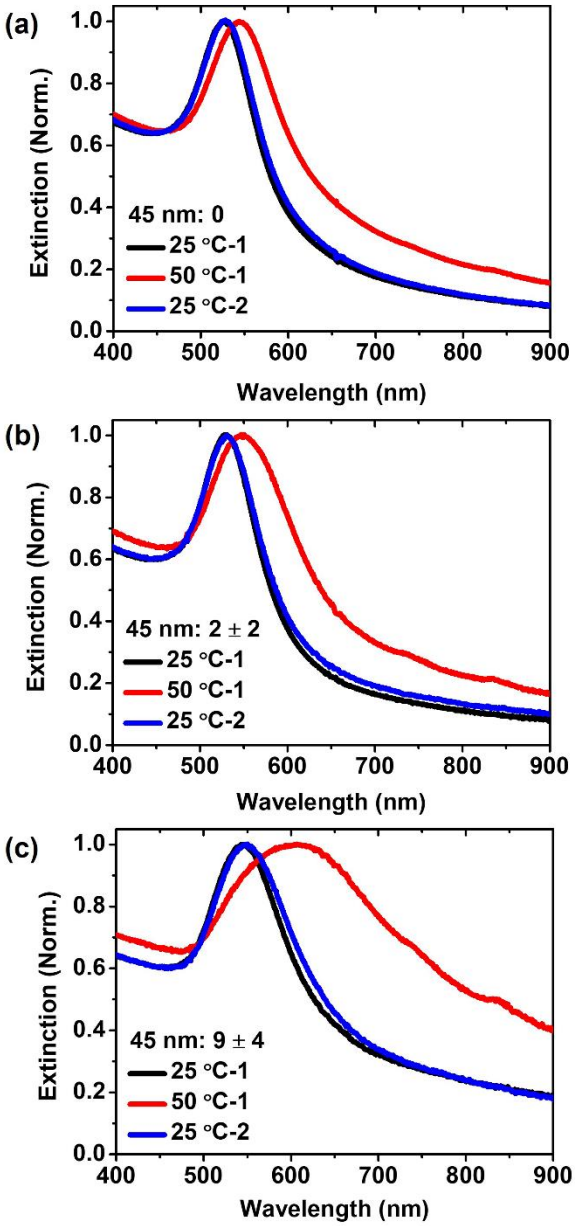

Figure S11. (a-c) Extinction spectra measured while varying the temperature from 25 °C (black) to 50 °C (red) and back to 25 °C (blue) for Au15/Au45 BMMs. The average number of 45 nm Au beads was measured to be 0 (a), 2 ± 2 (b), and 9 ± 4 (c).

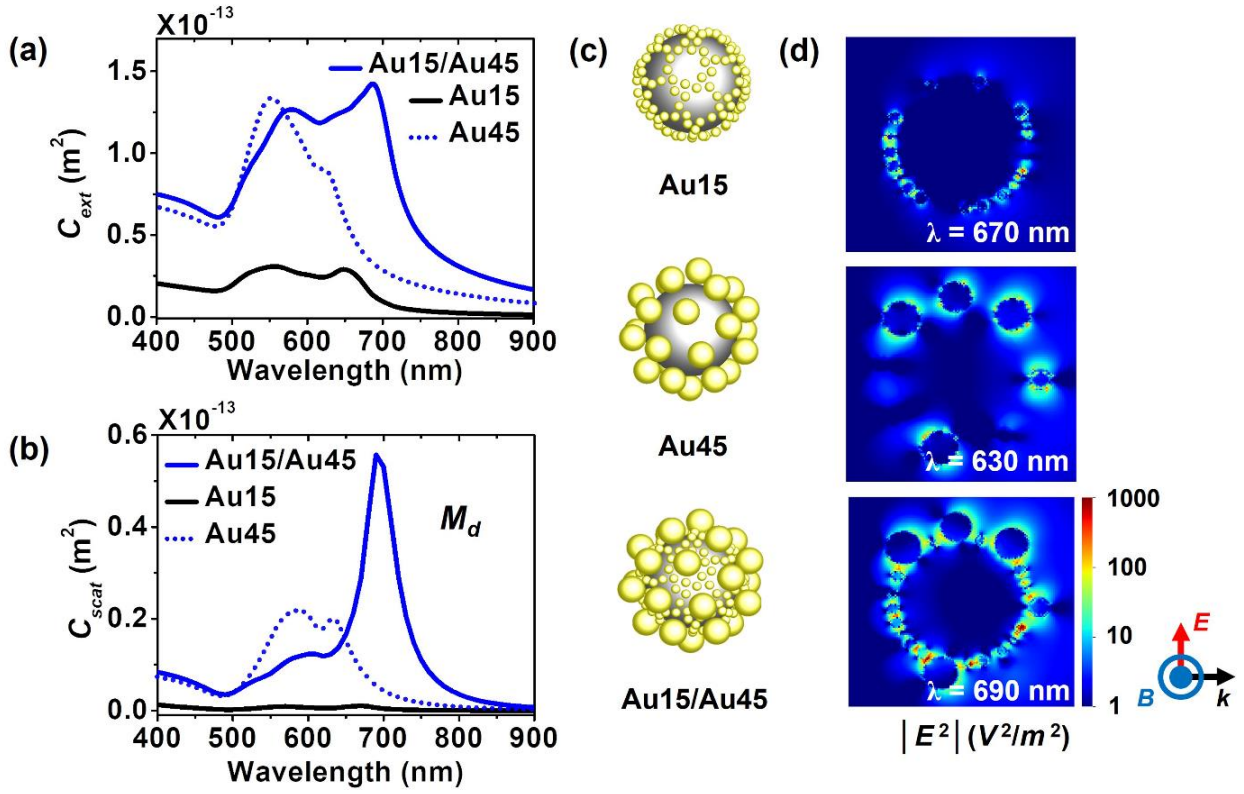

Figure S12. Simulated data of h-MMs generated by removing either all 45 nm beads (Au15 h-MM) or all 15 nm beads (Au 45 h-MM) along with those of Au15/Au45 h-BMM. (a-b) Simulated extinction spectra and scattering cross-section of the magnetic dipole mode of a Au15/Au45 h-BMM, a Au15 h-MM, and a Au45 h-MM. (c) Simulated models of a series of h-BMM and h-MMs. The simulation details are summarized in Table S3(1, 6-7). (d) Simulated near-field plot of $\left|\vec{E}\right|^2$ in log scale in the plane of $\vec{k}$ and $\vec{E}$ of a Au15 h-MM, a Au45 h-MM and a Au15/Au45 h-BMM at the magnetic dipole resonance. The wavelength in near-field map indicates the position of the magnetic dipole resonance for each model.

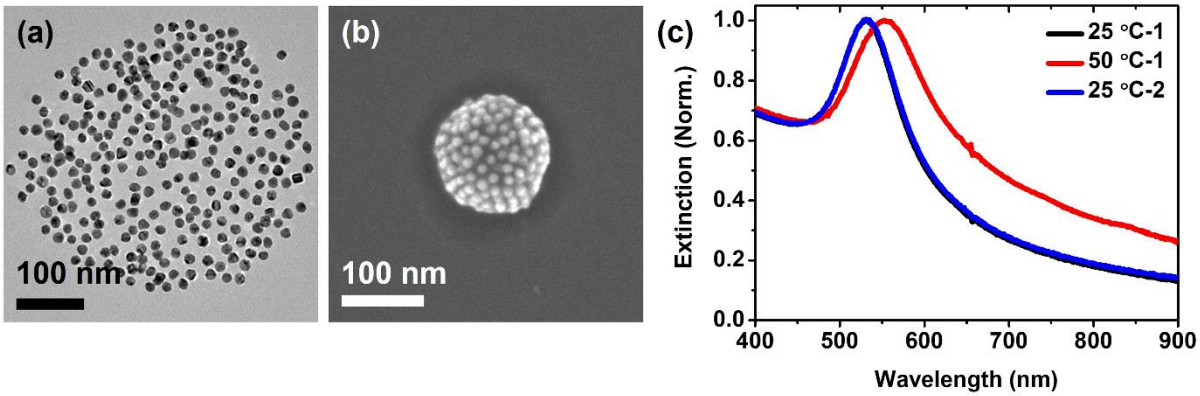

Figure S13. Au15 MMs constructed with 268 ± 16 of 15 nm beads, the largest number experimentally possible for 15 nm beads. (a) TEM images of Au15 l-MMs. (b) SEM images of Au15 h-MMs. (c) Extinction spectra measured while varying the temperature from 25 °C (black) to 50 °C (red) and back to 25 °C (blue) for Au15 MMs, showing that the bead size is too small to manifest strong magnetic resonances even at the high nanobead density achived in this study.

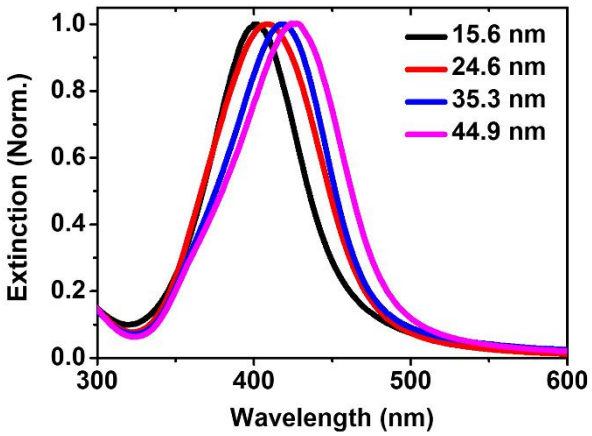

Figure S14. Extinction spectra of Ag nanobeads with various diameters.

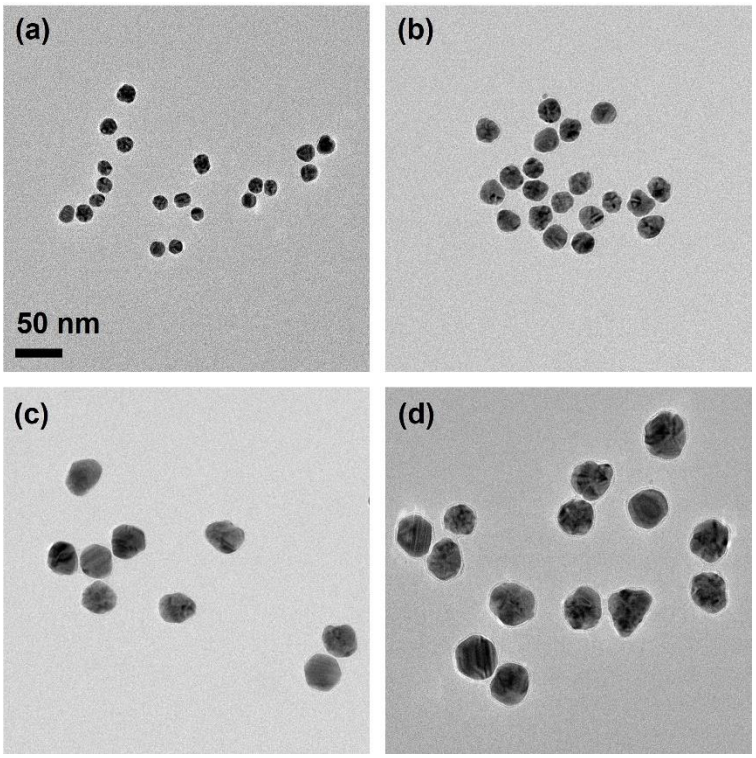

Figure S15. TEM images of Ag nanobeads with various diameters. The nanobead diameters were measured to be (a) 16 ± 2, (b) 25 ± 2, (c) 35 ± 2, and (d) 45 ± 3 nm.

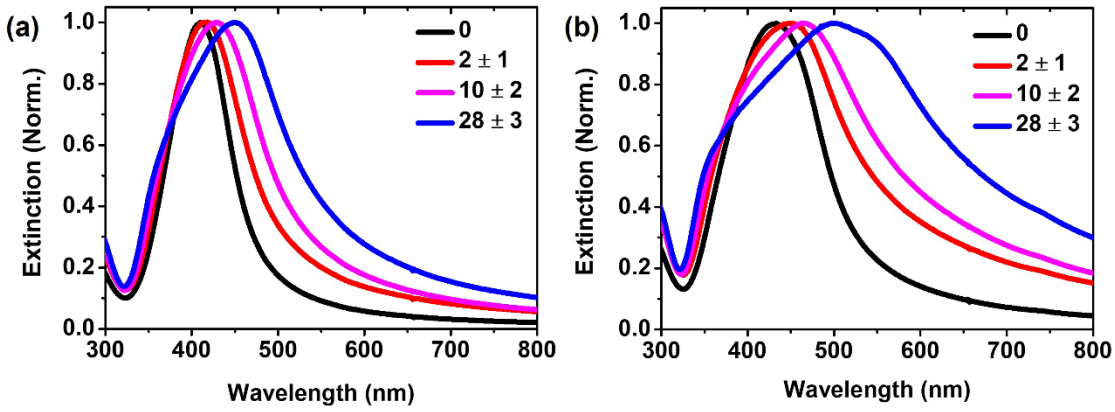

Figure S16. (a-b) Extinction spectra of Ag16/Ag45 l-BMMs (a) and Ag16/Ag45 h-BMMs (b) with 16 nm and 45 nm Ag beads. The legend indicates the number of 45 nm Ag beads. The average number of 16 nm Ag beads is 160.

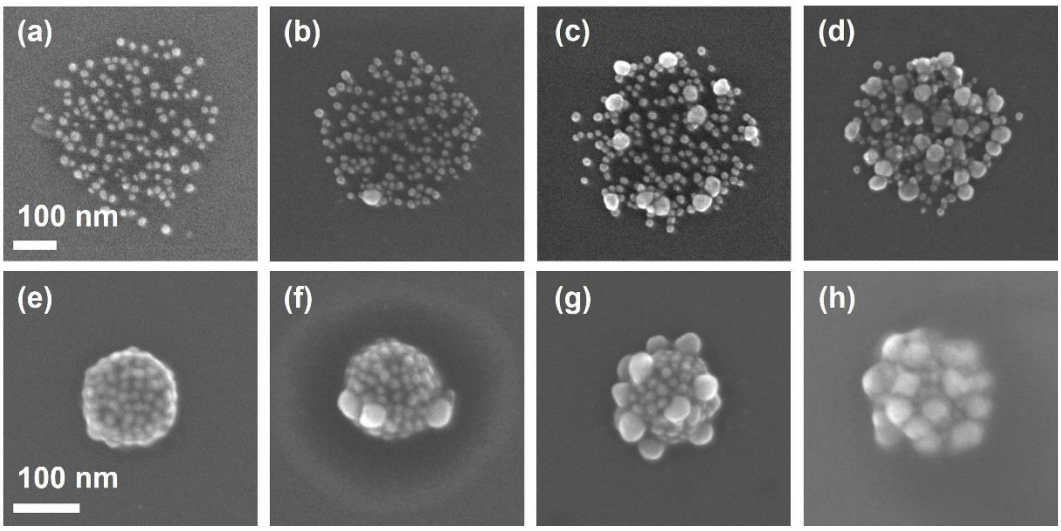

Figure S17. (a-h) SEM images of Ag16/Ag45 l-BMMs (a-d) and Ag16/Ag45 h-BMMs (e-h) constructed with two different diameters of nanobeads. The average number of 45 nm beads was measured to be 0 (a, e), 2 ± 1 (b, f), 10 ± 2 (c, g), and 28 ± 3 (d, h). Other structural parameters are summarized in Table S1(4-6) and Table S2(5).

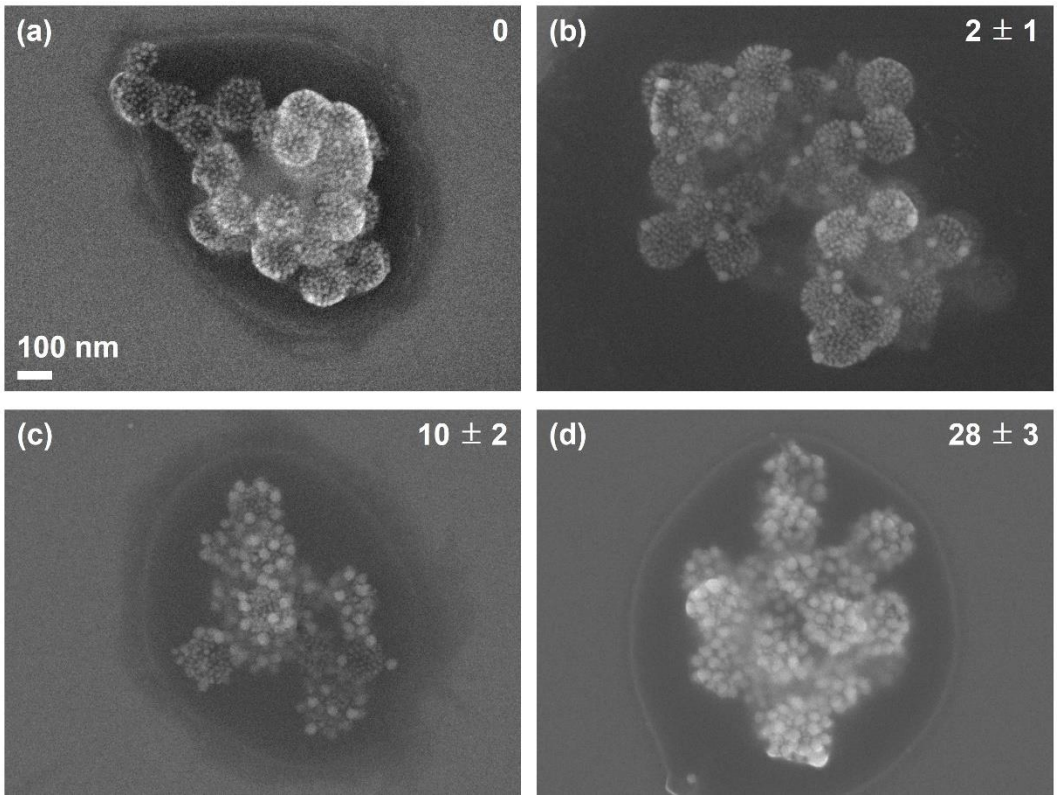

Figure S18. (a-d) SEM images Ag16/Ag45 h-BMMs with two different diameters of nanobeads. The numbers in the SEM images indicate the average number of 45 nm beads per core.

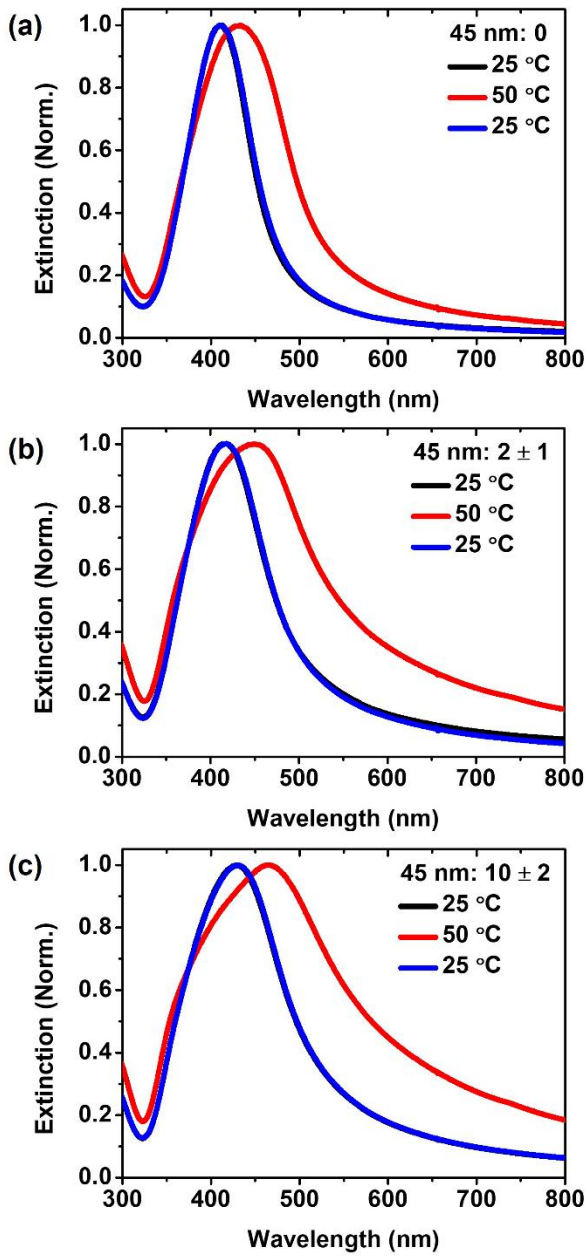

Figure S19. (a-c) The extinction spectra measured while varying the temperature from 25 °C (black) to 50 °C (red) and back to 25 °C (blue) for Ag16/Ag45 BMMs made of 16 and 45 nm beads. The average number of 45 nm beads was measured to be 0 (a), 2 ± 1 (b), and 10 ± 2 (c).

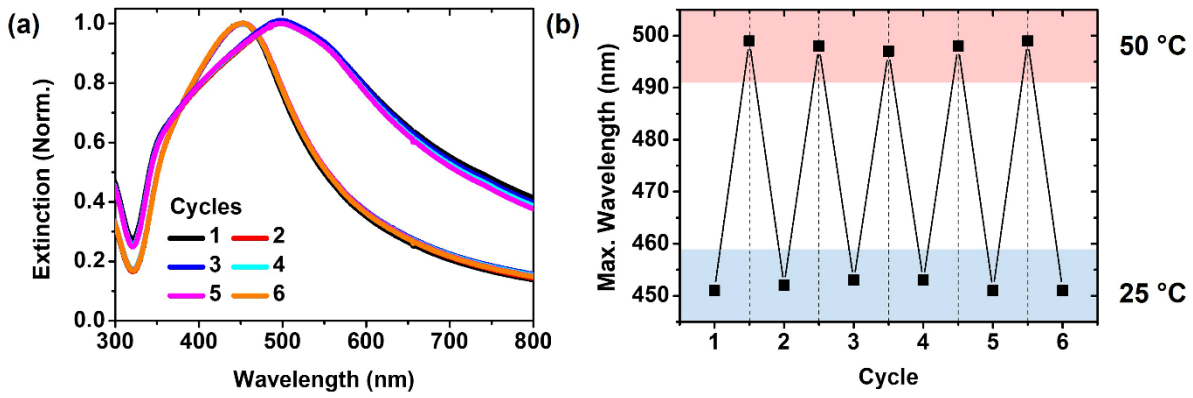

Figure S20. (a) Extinction spectra of Ag16/Ag45 BMMs with two different diameters of nanobeads measured with temperature cycling between 25 °C and 50 °C. (b) Extinction peak positions corresponding to temperature cycling as shown in a.

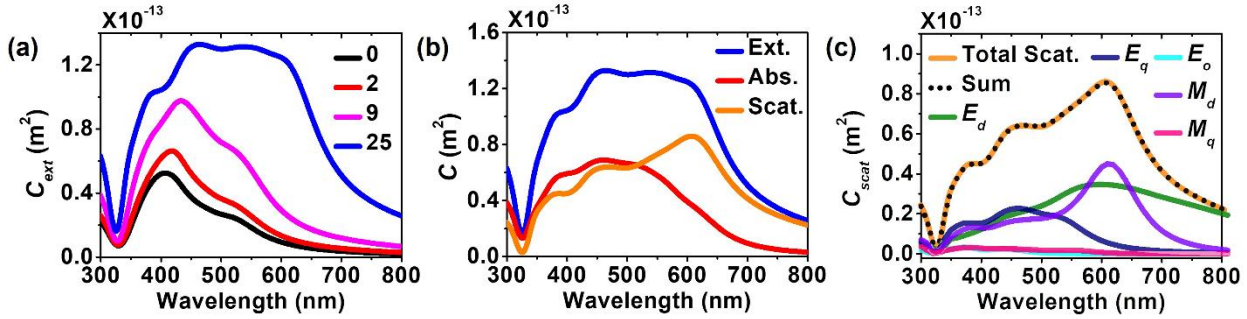

Figure S21. Optical analysis and simulation results for a Ag15/Ag45 h-BMM. Ag15/Ag45 BMM models have the same structural parameters as the Au versions shown in Table S3(1-4). (a) Simulated extinction spectra of Ag15/Ag45 h-BMMs with different numbers of 45 nm Ag beads. (b) Simulated extinction (blue), absorption (red), and scattering (orange) cross-sections of a modeled h-BMM with 15 nm and 45 nm Ag beads. (c) Calculated scattering cross-section of different electric and magnetic resonance modes (E_d: electric dipole, E_q: electric quadrupole, E_o: electric octupole, M_d: magnetic dipole, M_q: magnetic quadrupole). The sum (black dotted line) is over the cross-sections of all four calculated electric and magnetic modes. The total scattering spectrum (orange) directly obtained by FDTD simulation is also presented for comparison.

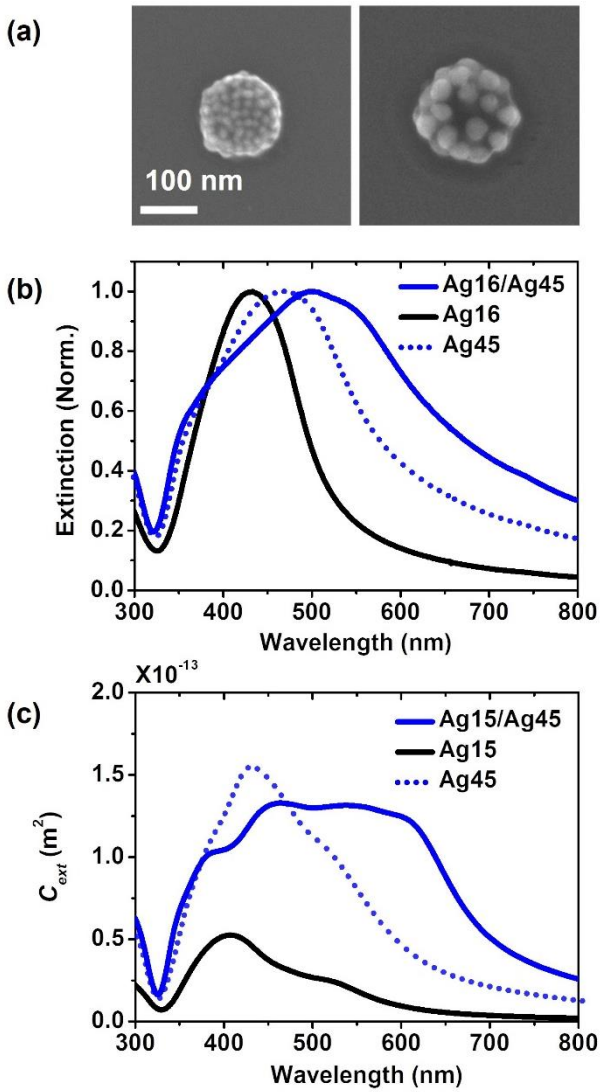

Figure S22. (a) SEM images of Ag16 h-MMs and Ag45 h-MMs constructed with 16 nm and 45 nm Ag beads. Other structural parameters are summarized in Table S2(5-6). (b) Experimental extinction spectra of Ag16 h-MMs, Ag45 h-MMs, and Ag16/Ag45 h-BMMs. (c) Corresponding simulated extinction spectra.

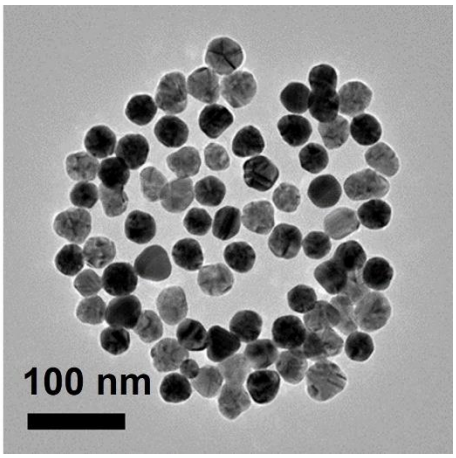

Figure S23. TEM image of Ag35/Au35 l-BMM, where Au nanobeads appear darker than Ag nanobeads.

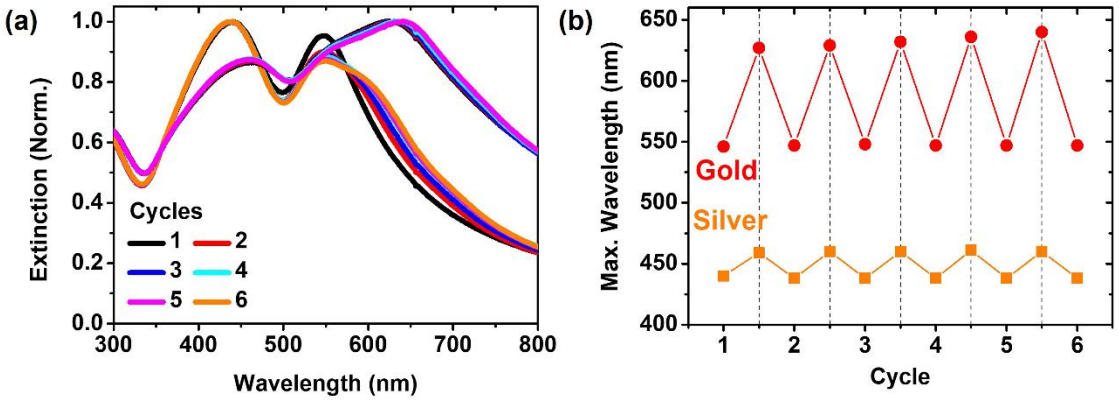

Figure S24. (a) Extinction spectra of Ag35/Au35 BMMs measured with temperature cycling between 25 °C and 50 °C. The structural details are summarized in Table S4(1). After repeated cycles of heating and cooling, a slight reorganization of each nanobead type is observed, which induces slight broadening of these resonances.

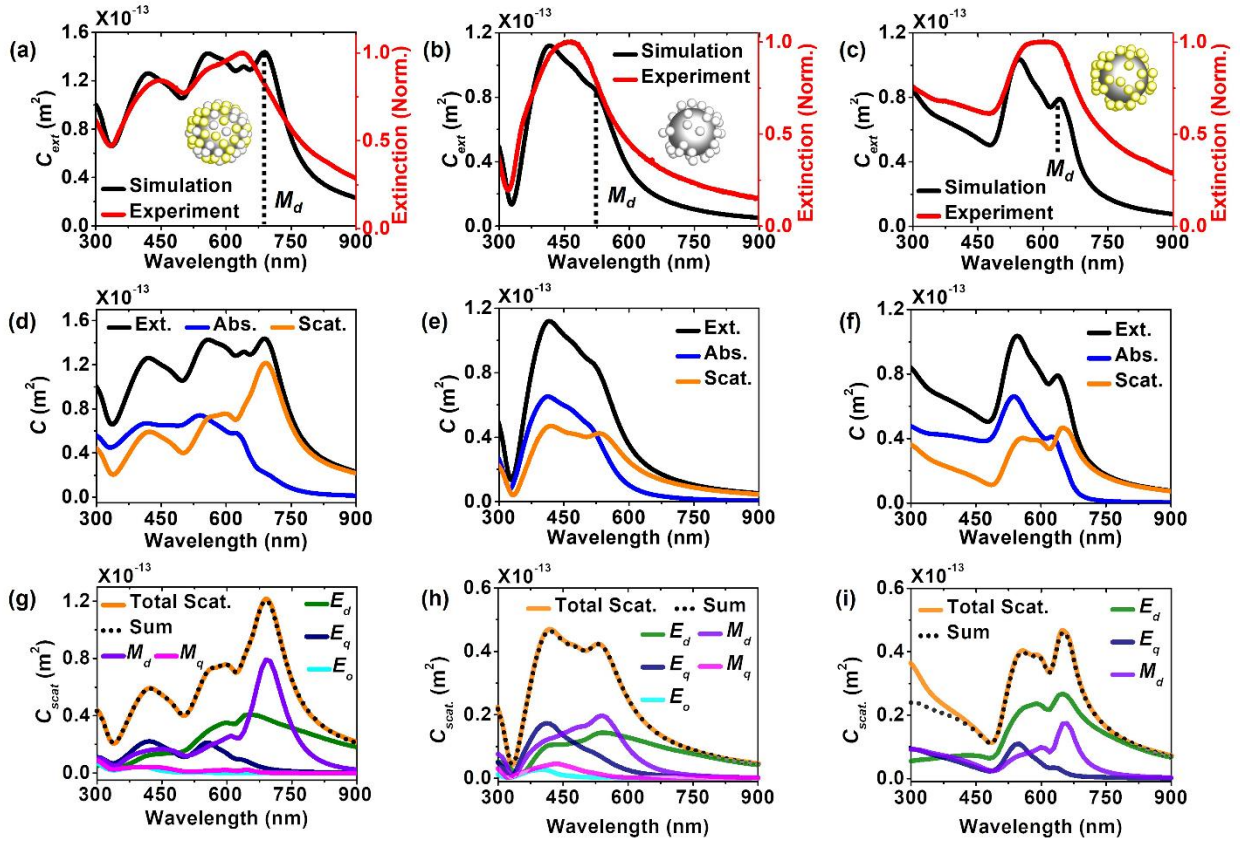

Figure S25. Optical analysis and simulation results for a Ag35/Au35 h-BMM, a Ag35 h-MM, and a Au35 h-MM. (a-c) Simulated and experimental extinction spectra of Ag35/Au35 h-BMM (a), a Ag35 h-MM (b), and a Au35 h-MM (c). The inset shows the structure of the simulation models. The position of the magnetic dipole (M_d) is marked for clarity. (d-f) Simulated extinction (black), absorption (blue), and scattering (orange) cross-sections of a modeled Ag35/Au35 h-BMM (d), Ag35 h-MM (e), and Au35 h-MM (f). (g-i) Calculated scattering cross-sections of electric and magnetic modes for a Ag35/Au35 h-BMM (g), a Ag35 h-MM (h), and a Au35 h-MM (i). The sum (black dotted line) is over the cross-sections of the calculated electric and magnetic modes. The total scattering spectrum (orange) directly obtained by FDTD simulation is also presented for comparison.

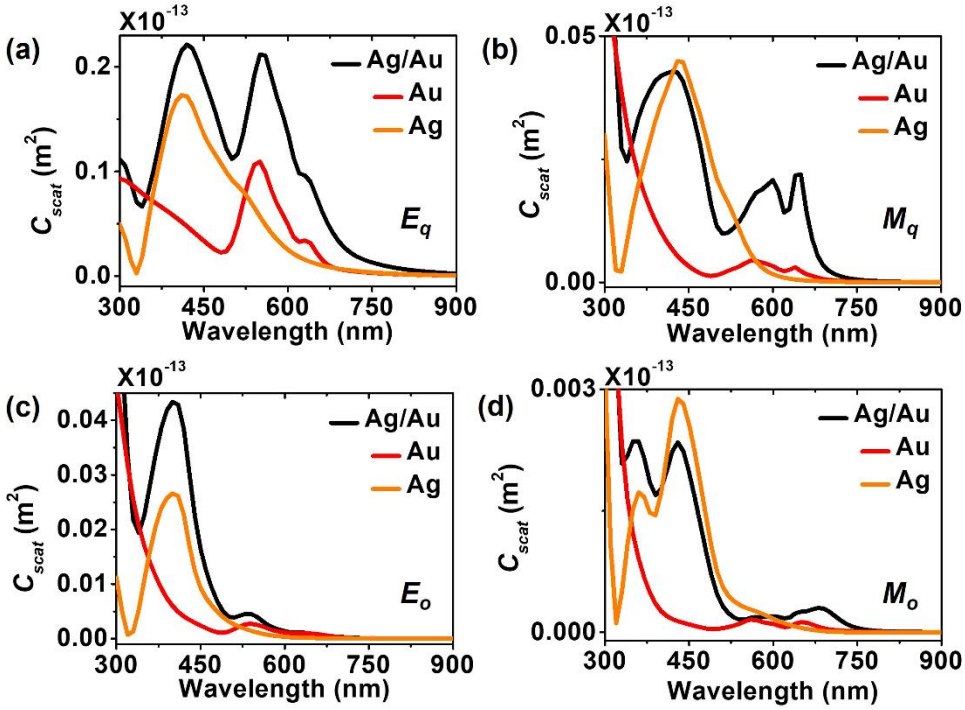

Figure S26. (a-d) Calculated scattering cross-sections of electric and magnetic modes in a Ag35/Au35 h-BMM (black), a Au35 h-MM (red), and a Ag35 h-MM (orange): (a) Electric quadrupole (E_q), (b) magnetic quadrupole (M_q), (c) electric octupole (E_o) and (d) magnetic octupole (M_o). The simulated parameters are provided in Table S5(1). Like the electric dipole mode, this coupling between Au and Ag beads does not appear to be significant for the electric quadrupole and octupole modes in Ag35/Au35 h-BMMs (a, c). On the other hand, Au and Ag nanobeads in Ag35/Au35 h-BMMs couple to each other, and this coupling contributes to the overall intensity and peak position of magnetic quadrupole and octupole modes at their resonant wavelengths (b, d).

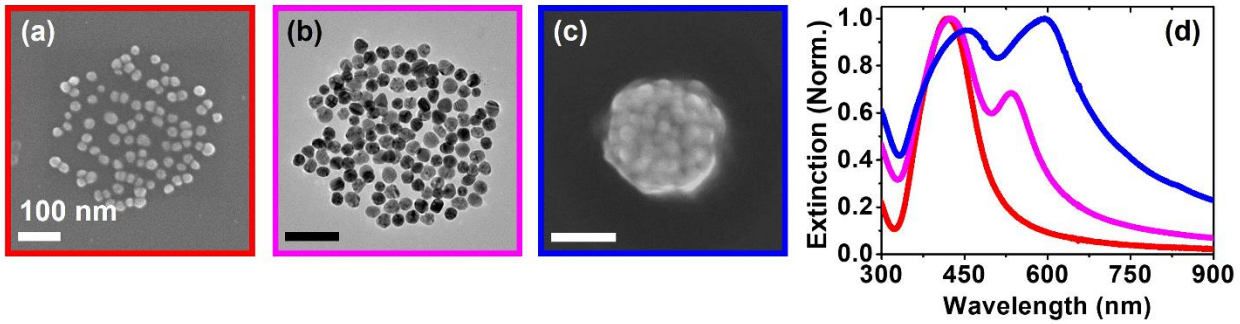

Figure S27. (a-c) Electron microscope (EM) images of a Ag25 l-MM, (a) a Ag25/Au25 l-BMM, (b) and a Ag25/Au25 h-BMM (c). All scale bars are 100 nm. (d) Extinction spectra of Ag25/Au25 BMMs following synthetic steps and temperature cycling. The structural details are summarized in Table S4(2).

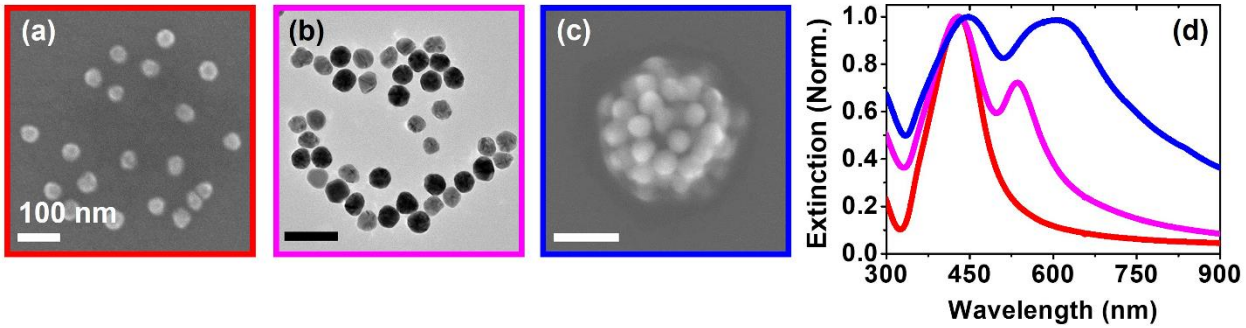

Figure S28. (a-c) EM images of a Ag45 l-MM (a), a Ag45/Au45 l-BMM (b), and a Ag45/Au45 h-BMM (c). All scale bars are 100 nm. (d) Extinction spectra of Au45/Ag45 BMMs following synthetic steps and temperature cycling. The structural details are summarized in Table S4(3).

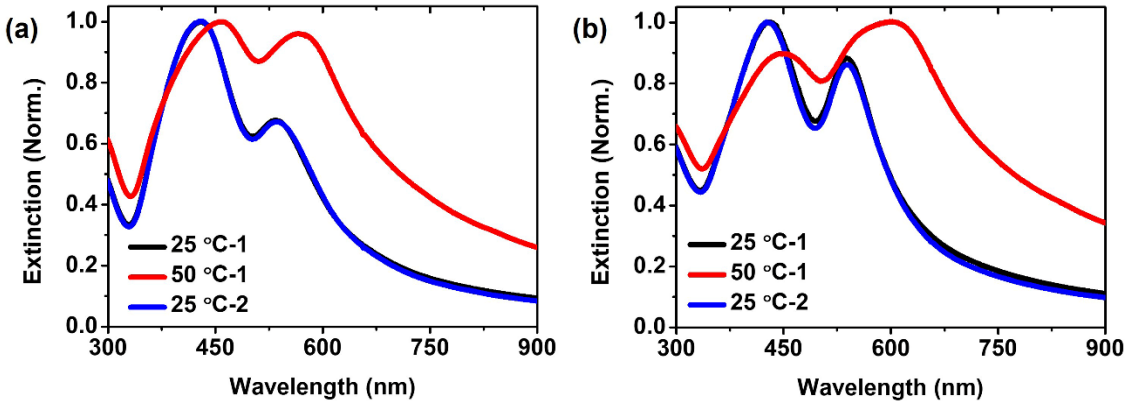

Figure S29. The extinction spectra of Ag25/Au25 BMMs (a) and Ag45/Au45 (b) measured with temperature cycling between 25 °C and 50 °C.

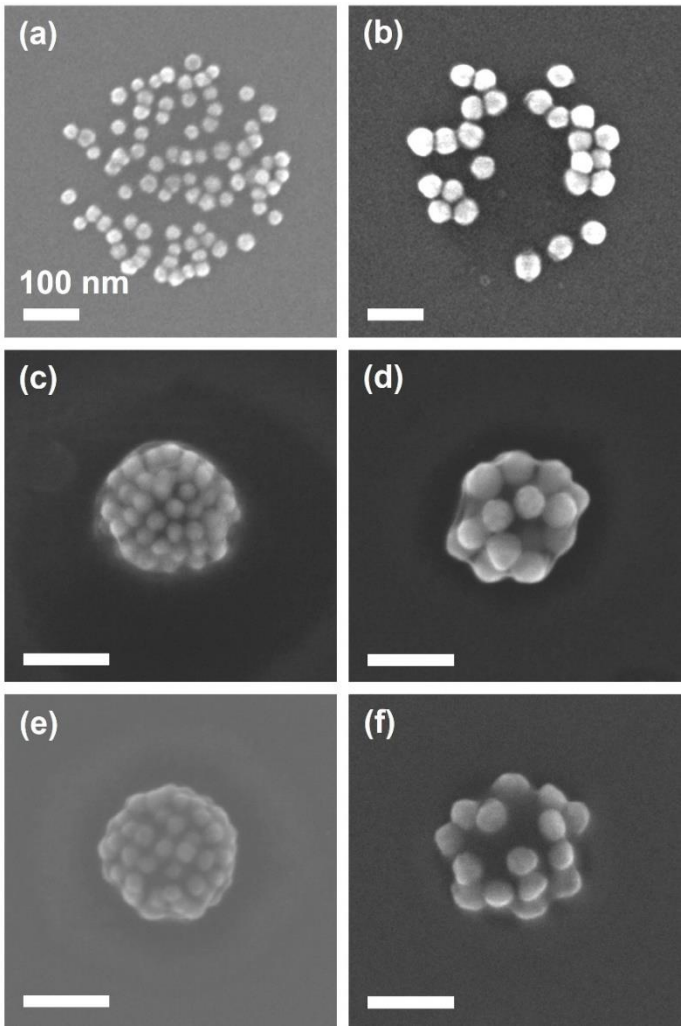

Figure S30. (a-d) SEM images of Au l-MMs (a-b) and Au h-MMs (c-d) made of 25 nm and 45 nm Au beads ((a, c) 25 nm, (b, d) 45 nm Au beads). (e-f) SEM images of Ag h-MMs composed of 25 nm (e) and 45 nm (f) Ag beads. The structural details are summarized in Table S2(9-12). All scale bars are 100 nm.

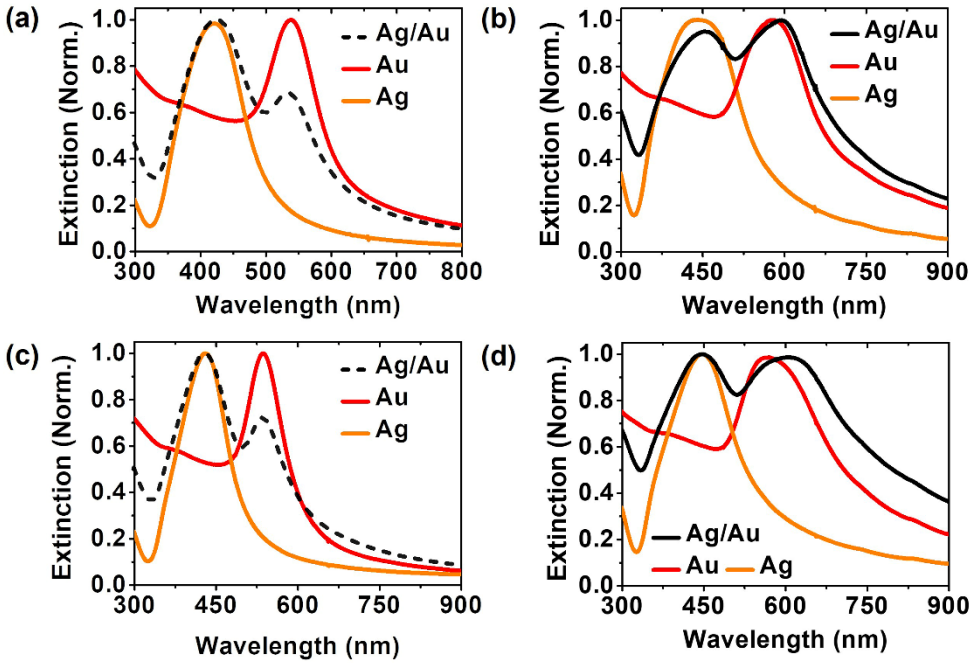

Figure S31. Experimental extinction spectra of Ag/Au BMMs (black), Au MMs (red) and Ag MMs (orange) at 25 °C and 50 °C. (a-b) Extinction spectra of Ag25/Au25 BMMs, Au25 MMs, and Ag25 MMs at 25 °C (a) and 50 °C (b). (c-d) Extinction spectra of Ag45/Au45 BMMs, Au45 MMs, and Ag45 MMs at 25 °C (c) and 50 °C (d). Structural details are listed in Table S2(9-12) and S4(2-3).

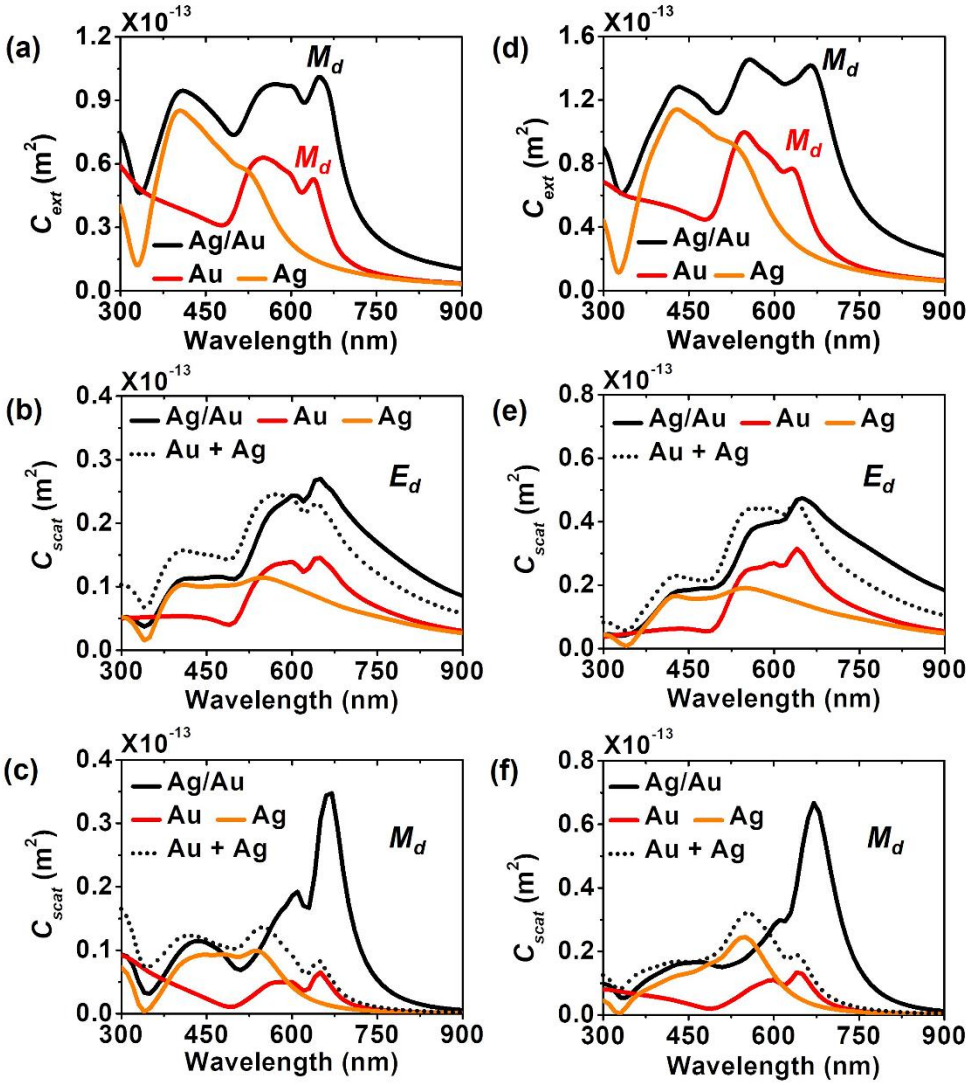

Figure S32. (a) Simulated extinction spectra of a Ag25/Au25 h-BMM (black), a Ag25 h-MM (red) and a Ag25 h-MM (orange). (b-c) Simulated scattering cross-section of the electric dipole (b) and magnetic dipole (c) of the series of models in a. (d) Simulated extinction spectra of a Ag45/Au45 h-BMMs (black), a Au45 h-MMs (red), and a Ag45 h-MM (orange). (e-f) Simulated scattering cross-section of the electric dipole (e) and magnetic dipole (f) of the series of models in d. The structural parameters for the simulations are summarized in Table S5(2-3) and Table S6(3-6). The black dotted line in b-c and d-e shows the sum of the cross-sections of Au h-MMs and Ag h-MMs for the electric and magnetic dipole modes, respectively.

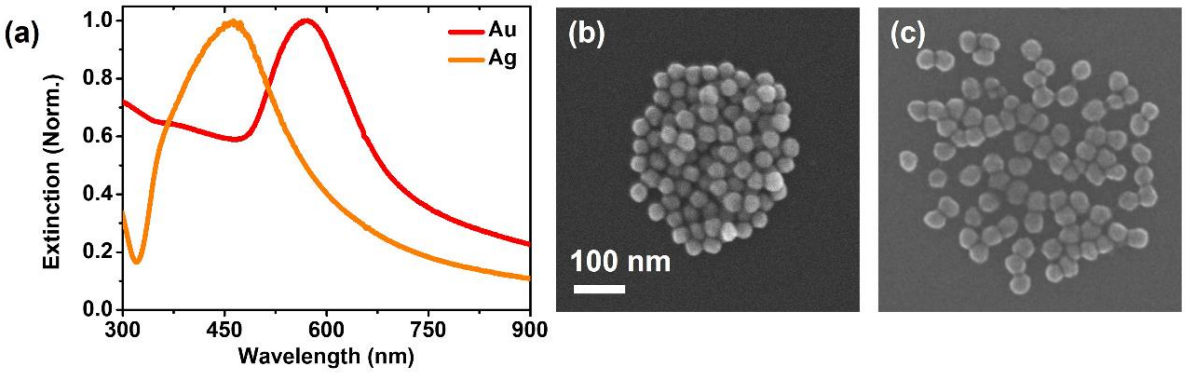

Figure S33. (a-c) Extinction spectra (a) and SEM images of Au35 l-MMs (b) and Ag35 l-MMs (c). The average diameter of Au and Ag beads is 35 ± 2 nm and 35 ± 2 nm. The average number of nanobeads on a core is 86 ± 6 for Ag35 MMs and 85 ± 7 for Au35 MMs. The structural details are summarized in Table S2(13-14). All scale bars share a 100 nm scale.

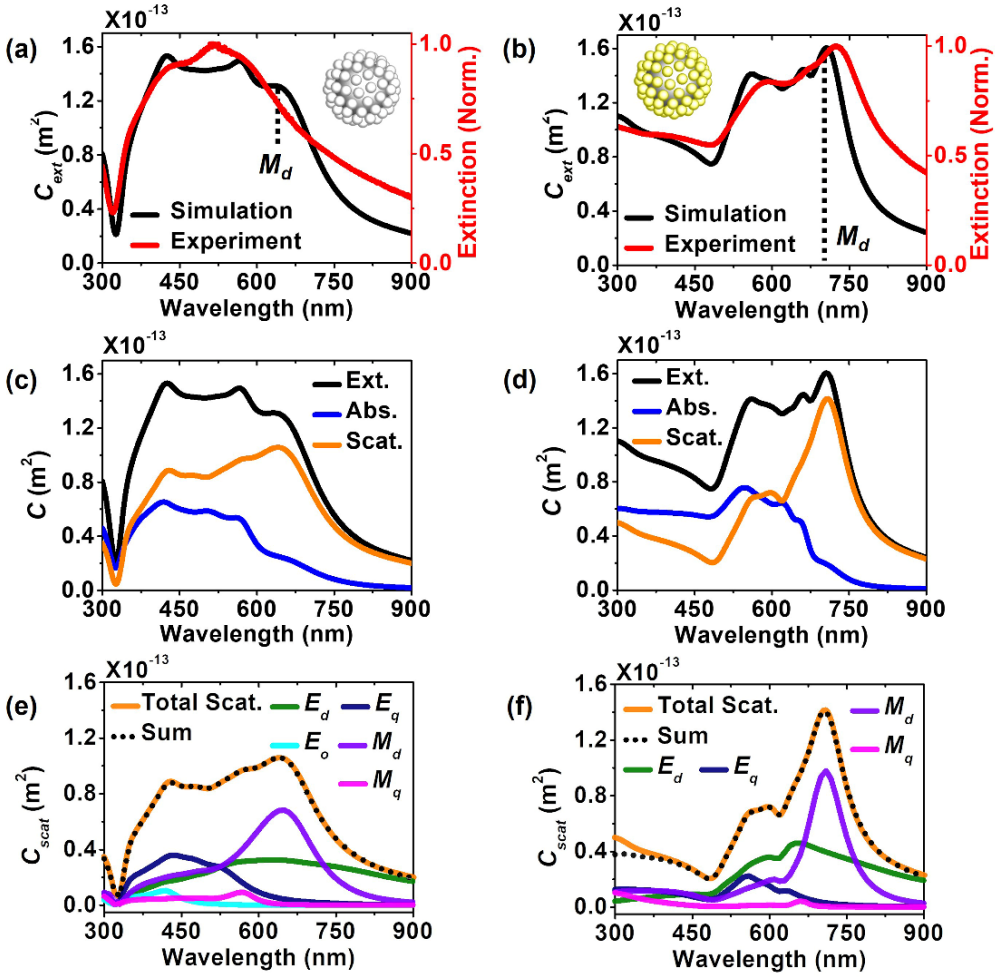

Figure S34. Optical analysis and simulation results for a Ag35 h-MM and a Au35 h-MM with 35 nm Au and Ag beads. (a-b) Simulated and experimental extinction spectra of a Ag35 h-MM (a) and a Au35 h-MM (b). The inset shows the cross-section of the simulated h-MM models, which is composed of 35 nm Ag beads and 35 nm Au beads. The structural parameters for the simulations are summarized in Table S6(7-8). The position of the magnetic dipole (M_d) is marked for clarity. (c-d) Simulated extinction (black), absorption (blue), and scattering (orange) cross-sections of a modeled Ag35 h-MM (c) and Au35 h-MM (d). (e-f) Calculated scattering cross-sections of electric and magnetic modes for a Ag35 h-MM (e) and a Au35 h-MM (f). The sum (black dotted line) is the cross-sections of the calculated electric and magnetic modes. The total scattering spectrum (orange) directly obtained by FDTD simulation is also presented for comparison.

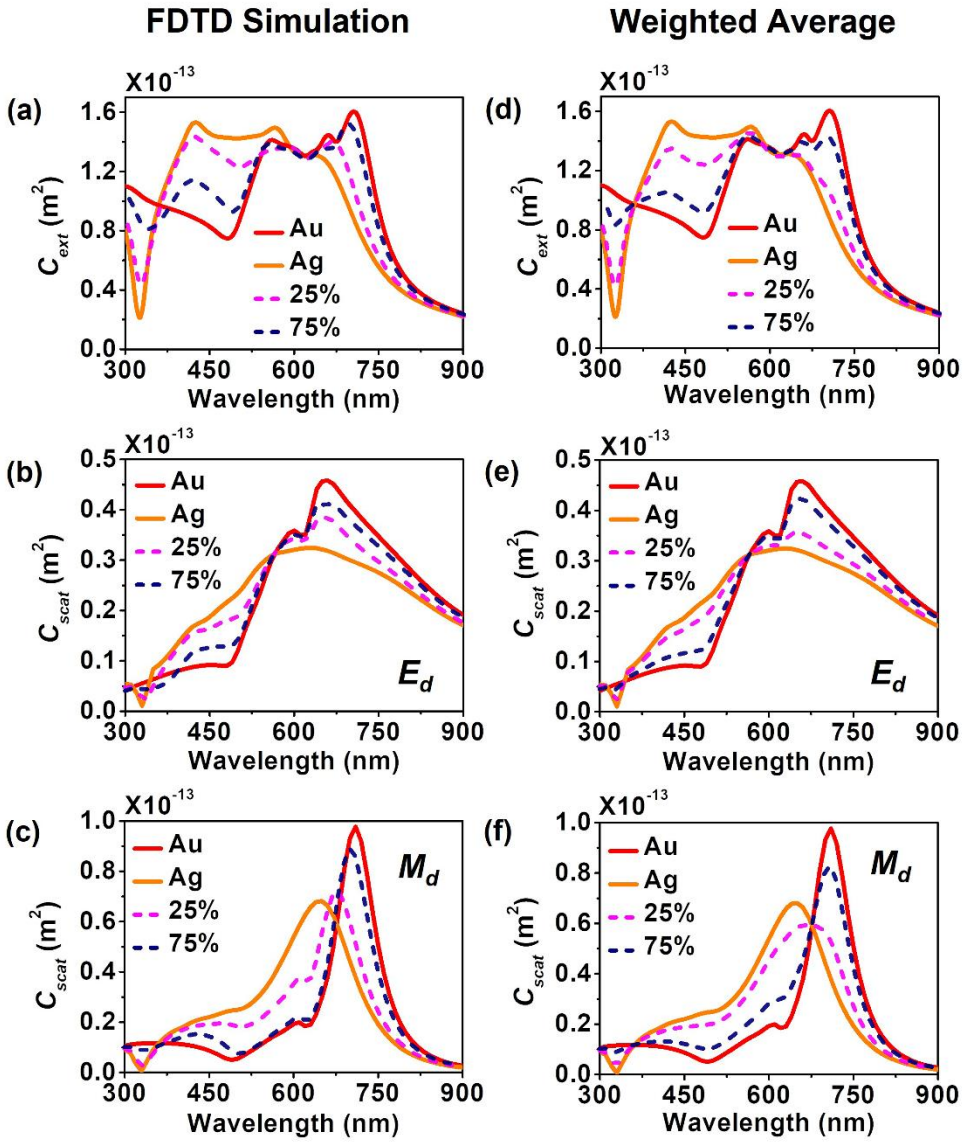

Figure S35. (a) Simulated extinction spectra of a Ag35/Au35 h-BMM with 62 Au nanobeads and 21 Ag nanobeads (indicated by the navy dashed line, 75% Au nanobeads), a Ag35/Au35 h-BMM with 21 Au nanobeads and 62 Ag nanobeads (indicated by the magenta dashed line, 25 % Au nanobeads), and the corresponding Au35 and Ag35 h-MMs. (b-c) The electric dipole (E_d, b) and magnetic dipole (M_d, c) scattering cross-section for a Au35/Ag35 h-BMM with 62 Au nanobeads and 21 Ag nanobeads, a Au35/Ag35 h-BMM with 21 Au nanobeads and 62 Ag nanobeads, and the corresponding Au35 and Ag35 h-MMs. Structural details in simulations are listed in Table

S5(4-5) and Table S6(7-8). (d-f) The weighted average extinction spectra (d) and scattering cross-section of the electric dipole (E_d, e) and magnetic dipole (M_d, f) of a Ag35/Au35 h-BMM with 62 Au nanobeads and 21 Ag nanobeads (indicated by the navy dashed line, 75% Au nanobeads) and a Ag35/Au35 h-BMM with 21 Au nanobeads and 62 Ag nanobeads (indicated by the magenta dashed line, 25 % Au nanobeads). These show the sum of the Au35 h-MM and Ag35 h-MM cross-sections weighted by the fraction of Au and Ag nanobeads. The spectra of the Au35 and Ag35 h-MMs presented in d-f are simulated spectra.

IV. References

1. Turkevich, J.; Stevenson, P. C.; Hillier, J., A Study of the Nucleation and Growth Processes in the Synthesis of Colloidal Gold. *Discuss. Faraday Soc.* **1951**, *11*, 55-75.

2. Bastús, N. G.; Comenge, J.; Puntes, V., Kinetically Controlled Seeded Growth Synthesis of Citrate-Stabilized Gold Nanoparticles of up to 200 nm: Size Focusing versus Ostwald Ripening. *Langmuir* **2011**, *27*, 11098-11105.

3. Bastús, N. G.; Merkoçi, F.; Piella, J.; Puntes, V., Synthesis of Highly Monodisperse Citrate-Stabilized Silver Nanoparticles of up to 200 nm: Kinetic Control and Catalytic Properties. *Chem. Mater.* **2014**, *26*, 2836-2846.

4. Lim, S.; Song, J. E.; La, J. A.; Cho, E. C., Gold Nanospheres Assembled on Hydrogel Colloids Display a Wide Range of Thermoreversible Changes in Optical Bandwidth for Various Plasmonic-based Color Switches. *Chem. Mater.* **2014**, *26*, 3272-3279.

5. Lee, S.; Woods, C. N.; Ibrahim, O.; Kim, S. W.; Pyun, S. B.; Cho, E. C.; Fakhraai, Z.; Park, S.-J., Distinct Optical Magnetism in Gold and Silver Probed by Dynamic Metamolecules. *J. Phys. Chem. C* **2020**, *124*, 20436-20444.

6. Tsang, L.; Kong, J. A.; Ding, K.-H., *Scattering of Electromagnetic Waves: Theories and Applications*; John Wiley & Sons, Inc.: USA, 2000.

7. Hastings, S. P.; Qian, Z.; Swanglap, P.; Fang, Y.; Engheta, N.; Park, S.-J.; Link, S.; Fakhraai, Z., Modal Interference in Spiky Nanoshells. *Opt. Express* **2015**, *23*, 11290-11311.

8. Fruhnert, M.; Fernandez-Corbaton, I.; Yannopapas, V.; Rockstuhl, C., Computing the T-matrix of a Scattering Object with Multiple Plane Wave Illuminations. *Beilstein J. Nanotechnol.* **2017**, *8*, 614-626.